ResearchGate

See discussions, stats, and author profiles for this publication at: https://www.researchgate.net/publication/350613751

# Wetting/Non-wetting behaviour of quadrupolar molecules (N2, C2H4, CO2) on Planar Substrates

**Article** *in* Chemical Engineering Journal · April 2021

DOI: 10.1016/j.cej.2021.129502

CITATIONS
0

READS
40

**4 authors**, including:

Hui Xu
The University of Queensland
**13** PUBLICATIONS **60** CITATIONS
SEE PROFILE

Krittamet Phothong
Suranaree University of Technology
**2** PUBLICATIONS **0** CITATIONS
SEE PROFILE

David Nicholson
The University of Queensland
**351** PUBLICATIONS **7,501** CITATIONS
SEE PROFILE

**Some of the authors of this publication are also working on these related projects:**



Characterization View project



Molecular hydrodynamics View project

All content following this page was uploaded by Krittamet Phothong on 26 April 2021.

The user has requested enhancement of the downloaded file.

Chemical Engineering Journal 419 (2021) 129502

Contents lists available at ScienceDirect

Chemical Engineering Journal

journal homepage: www.elsevier.com/locate/cej

# Wetting/non-wetting behaviour of quadrupolar molecules ($N_2$, $C_2H_4$, $CO_2$) on planar substrates

Hui Xu [a], Krittamet Phothong [a,b], D.D. Do [a,*], D. Nicholson [a]

[a] School of Chemical Engineering, University of Queensland, St Lucia, QLD, 4072, Australia
[b] School of Chemical Engineering, Institute of Engineering, Suranaree University of Technology, Nakhon Ratchasima, 30000, Thailand

ARTICLE INFO

*Keywords:*
Wetting
Non-wetting
Quadrupole moment
Nitrogen
Ethylene
Carbon dioxide
Adsorption

ABSTRACT

Molecular simulations were carried out to evaluate the performance of intermolecular potential models for the adsorbates: nitrogen, ethylene and carbon dioxide with leading quadrupoles. Models having only LJ interactions, are compared with the corresponding multi-site models with partial charges for their performance in describing the experimental data for vapour-liquid equilibrium (*VLE*), adsorption isotherms and isosteric heat of adsorption on planar adsorbent substrates. It is found that the models with partial charges outperform models using only LJ atoms for the description of adsorption, highlighting the important role of the quadrupole moment in a non-uniform adsorbed phase. These models were then used to construct the wetting maps of nitrogen, ethylene and carbon dioxide as a function of the temperature and the strength of the planar substrate to show the influence of the quadrupole moment on the behaviour of non-wetting/partial wetting/complete wetting at the coexistence pressure of the bulk phase.

## 1. Introduction

Adsorption of gases on graphitized thermal carbon black (GTCB) has been extensively studied because this solid possesses an energetically homogeneous surface and is ideal to characterize the intrinsic interaction between adsorbate and the surface. They also have relevance to the adsorption behaviour of carbon adsorbents used in practice. Adsorbates can form either molecular layers or clusters on the surface, depending on the interplay of the various potential energy interactions in the system. To understand the growth mode of the adsorbed film or the behaviour of clusters on the surface, extensive studies were carried out to investigate the phenomenon of wetting/non-wetting on GTCB, for example Ar [1–2], Kr [3–4], Xe [5], quadrupolar adsorbates, $N_2$ [6], and $C_2H_4$ [7], $CO_2$ [8], and polar adsorbates such as $H_2O$ [9–10], $NH_3$ [11], $C_2Cl_2F_4$ [12], $CH_2Cl_2$ [13]. A number of theories on wetting/non-wetting have been proposed in the literature [14–19], and because of the different terminologies used in different scientific disciplines to describe the same phenomena we provide brief definitions of the various terms in Table 1 to give clarity to the subsequent discussion. It is known that wetting/non-wetting is governed by the interplay between the adsorbate intermolecular interactions, the adsorbate-adsorbent interactions and the temperature [17,20]. However, the role of molecular dipole moments and quadrupole moments on wetting/non-wetting behaviour in adsorption has not been sufficiently quantified. Terlain and Larher [21] reported isotherms for $CO_2$, $N_2O$ and $C_2N_2$ adsorption on graphite, and found the quadrupole moment strongly favours an ordering orientation within the adsorbate, and as such a question is raised about its role in wetting/non-wetting phenomena.

Fig. 1 compares the strength of the quadrupoles for the adsorbates chosen in this investigation with argon as the reference. For these adsorbates, we chose a number of potential models: Single LJ-site, Two-LJ-site, and Multi-Site with fixed partial charges to illustrate not only the role of the quadrupole moment but also the molecular shape on the adsorption/wetting behaviour. Computer simulations of vapour liquid equilibria and adsorption of $N_2$, $C_2H_4$ and $CO_2$ on graphite have been carried out to evaluate these models against the experimental data and simulations for the adsorption of these gases on planar substrates having different affinities. The results have been used to construct wetting maps and compare these with maps for non-polar argon.

* Corresponding author.
*E-mail address:* d.d.do@uq.edu.au (D.D. Do).

https://doi.org/10.1016/j.cej.2021.129502
Received 4 February 2021; Received in revised form 18 March 2021; Accepted 20 March 2021
Available online 3 April 2021
1385-8947/© 2021 Elsevier B.V. All rights reserved.

**Table 1**
Definitions of the various terms used.

| Term | Definition |
|---|---|
| Bulk coexistence pressure | The bulk coexistence pressure ($P_0$) refers to the saturation pressure for vapour-liquid equilibrium at temperatures above the bulk triple point temperature, or the sublimation pressure for vapour-solid equilibrium at temperatures below the bulk triple point temperature. |
| Non-wetting | The adsorbate sparsely covers the surface at the bulk coexistence pressure ($P_0$). Typically, the adsorbed density at $P_0$ is less than the statistical monolayer density. |
| Incomplete wetting | A system is called incomplete wetting when the adsorbate forms a film of finite thickness at $P_0$. This is called Type 2 [24] or Stranski-Krastanov growth [25] in the colloid science literature. |
| Complete wetting | A system is called complete wetting when the adsorbed density tends to infinity when the pressure approaches $P_0$. This is called Type 1 [24] or Frank-van der Merwe growth [25]. |
| Wetting temperature/ layering temperature | The temperature at which there is a first order transition in the adsorbed density at $P_0$. If this transition leads to complete wetting (i.e. the adsorbed density tends to infinity) the temperature is denoted as the wetting temperature $T_W$. If a new layer n, is formed on top of an adsorbed film the temperature of layer formation is called the layering temperature of the n-th layer, $T_{L,n}$. |
| Roughening temperature | The temperature, denoted as $T_R$, which demarcates the wetting region from the incomplete wetting region. Above $T_R$ ,the interface between the adsorbed film and the gas phase becomes sufficiently undulated such that complete wetting occurs, otherwise incomplete wetting occurs at temperatures less than $T_R$. |

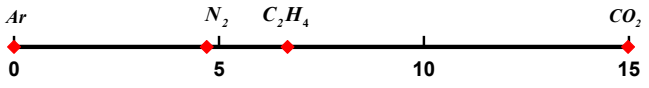


**Fig. 1.** The absolute value of the quadrupole moment ($10^{-40}$ C m$^2$) for Ar(0), $CO_2$(14.98) [22], $N_2$(4.70) [23] and $C_2H_4$(6.67) [23].

## 2. Theory

### 2.1. Kinetic Monte Carlo

The kinetic Monte Carlo (kMC) method was used in this study because of its distinct advantage of determining the chemical potential accurately [26], and has been successfully used to describe vapour-liquid equilibria [27] and adsorption [26,28]. Simulations were carried out with the substrate positioned at the bottom of a rectangular simulation box and a hard wall at the top of the box. Periodic boundary conditions were applied in the *x*- and *y*- directions, in the plane of the substrate. $10^8$ configurations were sampled in each of the equilibration and production stages.

### 2.2. Grand Monte Carlo simulation

Grand ensemble Monte Carlo simulation (GCMC) with the Metropolis scheme was used in simulations to derive the wetting map with one billion configurations each in the equilibration stage and in the production stage. A new configuration in the Markov chain, was selected from displacement, insertion or deletion with equal probability. In the equilibration stage, the maximum displacement length was initially set as half of the smallest dimension of the box and adjusted to achieve an acceptance ratio of 20%, and then kept constant in the production stage.

The surface excess, the isosteric heat, the orientation distribution and the local density distribution obtained from the simulation are defined in ***Appendix A***.

**Table 2**
Molecular Parameters of adsorbates used in this study.

| | Model | Atom | σ(nm) | $\varepsilon_{ff}/k_B(K)$ | q(e) | Geometry |
|---|---|---|---|---|---|---|
| Ar | M−Ar [29] | Ar | 0.3405 | 119.8 | 0 | – |
| $N_2$ | 2LJ + 3Q [31] | N | 0.331 | 36.0 | −0.482 | $l(N-N)$ = 0.110*nm* |
| | | COM* | 0.0 | 0.0 | 0.964 | |
| | 1CLJ [30] | – | 0.3615 | 101.5 | 0 | 0 |
| $C_2H_4$ | 2LJ + 4Q [33] | $CH_2$ | 0.3575 | 99.8 | 0.32 | $l(C-C)$ = 0.170*nm* |
| | | ** | – | – | −0.32 | $l(q-q)$ = 0.130*nm* |
| | 2LJ [32] | $CH_2$ | 0.3675 | 85 | 0 | $l(C-C)$ = 0.133*nm* |
| $CO_2$ | 3LJ + 3Q [31] | C | 0.28 | 27.0 | 0.7 | $l(C-O)$ = 0.116*nm* |
| | | O | 0.305 | 79.0 | −0.35 | |
| | 1CLJ [35] | – | 0.36481 | 246.15 | 0 | – |

* COM = centre of mass; **: the partial charges are on the line perpendicular to the C–C bond.

### 2.3. Fluid-Fluid ($U_{FF}$) and Solid-Fluid ($U_{SF}$) interaction energies

The molecular parameters for the potential models used to describe the Ar, $N_2$, $C_2H_4$, and $CO_2$ interactions, are listed in Table 2. The model for argon is taken from Michels [29], and denoted as M−Ar. Nitrogen was modelled either as a single *LJ* molecule (1CLJ $N_2$) [30] or as two-*LJ* sites with three fixed partial charges (2LJ + 3Q $N_2$) [31]. Ethylene was modelled as a two-site *LJ* model (2LJ $C_2H_4$) [32] or by the two-*LJ* sites and four partial charges (2LJ + 4Q $C_2H_4$) [33]. The single *LJ*-site model of $C_2H_4$ was not chosen here because it fails to describe the experimental vapour-liquid equilibria (VLE) [34]. $CO_2$ is modelled with either a single *LJ* site model (1CLJ $CO_2$) [35] or with three *LJ*-sites plus three partial charges (3LJ + 3Q $CO_2$) [31].

We use the ratio of the minimum of the solid–fluid ($u_{SF}$) potential energy profile to the minimum of the fluid–fluid ($u_{FF}$) potential energy profile, $D^*$, to define the relative strength of an adsorbent with respect to a given adsorbate:

$$D^* = \left|u_{SF,min}\right| / \left|u_{FF,min}\right| \quad (1)$$

The intermolecular energy was calculated as the sum of all pairwise interaction energies with the cross molecular parameters computed from the Lorentz-Berthelot mixing rules. The minimum fluid–fluid potential energy of a pair of adsorbate molecules is calculated as a function of the separation distance between their centres of mass. For a given separation, both molecules were given $10^6$ random orientations, and the minimum energy from the set of pairwise potential energies was recorded for this separation. These energies were then plotted against separation distance, and the minimum of this potential profile, $u_{FF,min}$, used in *eq.* (1).

The solid–fluid potential energy between an *LJ* site and a planar graphite substrate, modelled as a continuum solid, was calculated from the 10–4-3 potential equation [36], as a function of the separation distance in the *z*- direction between the centre of mass of a given adsorbate and the solid surface.

The adsorption strength of a substrate is denoted by the parameter $D_{ss}(K) = \rho_s \sigma_{ss}^2 \varepsilon_{ss}$, which only depends on the molecular properties of the substrate. For graphite, $D_{ss}$ = 124 K using the standard values $\varepsilon_{ss}$ = 28 K and σ = 0.34 nm and ρ = 38.2 nm$^{-2}$. To model planar substrates of different surface affinity, we varied the well-depth of the interaction energy, $\varepsilon_{ss}/k_B$.

## 3. Results and discussion

Simulations with the various intermolecular potentials listed in

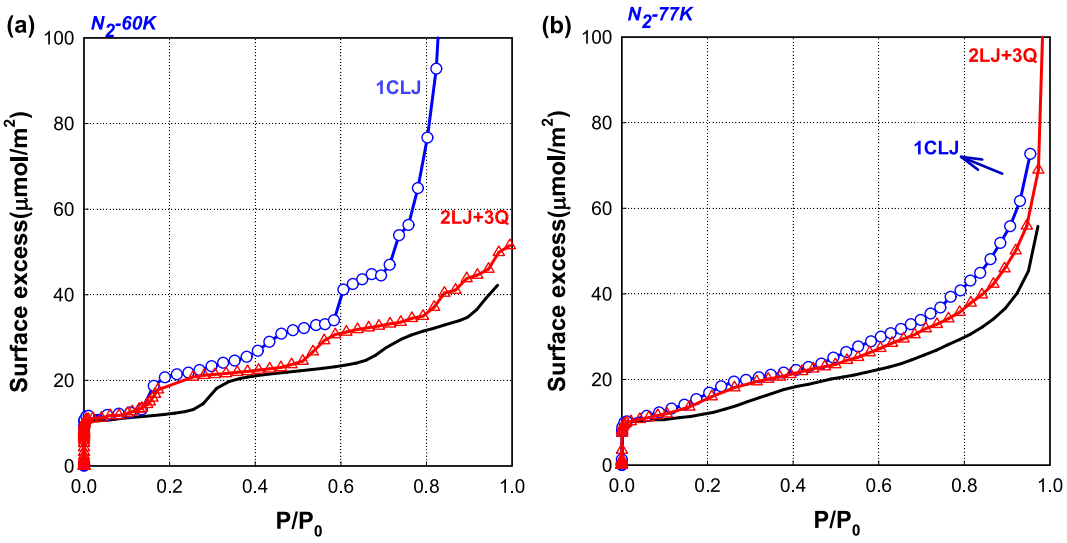


**Fig. 2.** Simulated isotherms with 1CLJ and 2LJ + 3Q for $N_2$ adsorption at 60 K (a) and 77 K (b) on graphite. Experimental data [37] is shown as the black solid line. Values of $P_0$ are given in Table 8.

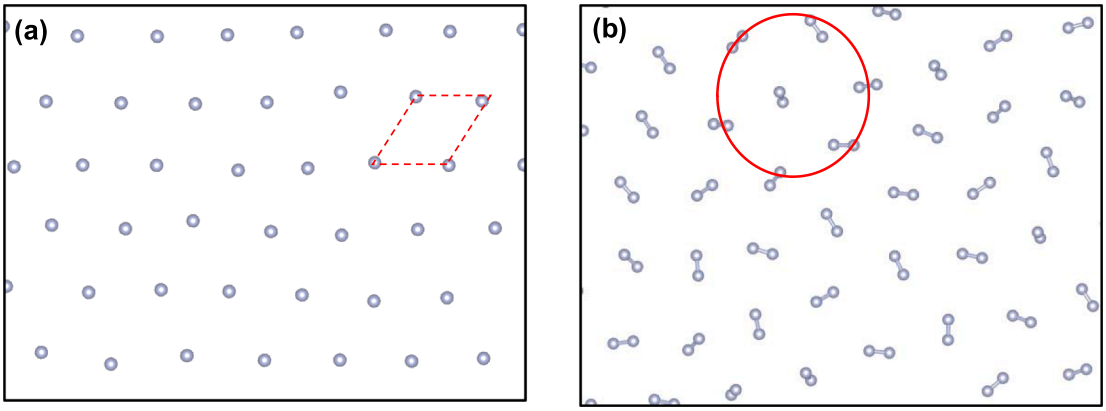


**Fig. 3.** Snapshots of molecular configurations for nitrogen with (a) 1CLJ model and (b) 2LJ + 3Q model at 60 K and 700 Pa. The red circle encloses a "pinwheel" cluster.

Table 2 generally give good agreement with experiment for the vapor–liquid equilibria (Fig. 17, Fig. 18, Fig. 19), with the models that account for shape and quadrupole moment performing slightly better. We next consider their performance in the description of isotherm and isosteric heat for adsorption on graphite.

### 3.1. Adsorption on graphite

$N_2$

The simulated isotherms and the experimental data [37] for $N_2$ adsorption on graphite at 60 K and 77 K are shown in Fig. 2 to illustrate the difference in the adsorption behaviour below and above the bulk triple point temperature of 63 K.

The 2LJ + 3Q $N_2$ model with partial charges describes the experimental data at 60 K and 77 K better than the 1CLJ model which is particularly poor at 60 K, where the molecular shape and quadrupole moment play a significant part in determining the packing of the structured first layer and consequently have a propagation effect in building the higher layers. The 1CLJ model over-predicts the adsorbed density at higher loadings because the 1CLJ molecules pack more efficiently than linear molecules as a CP 2D layer. The configuration snapshots of the monolayer at 60 K in Fig. 3 illustrate the differences in packing for the two models.

The regular hexagonal pattern of the 1CLJ molecules, provides adsorption sites at the centres of three adjacent molecules, on which molecules adsorb to form the second layer. This regular makes the second layer adsorption sites stronger, and as a result the 1CLJ model over-predicts the adsorbed density, compared to the experimental data. On the other hand, the 2LJ + 3Q model provides a more irregular monolayer structure, with pinwheel formations [38–39] in which a central molecule is oriented normal to the surface and its six nearest molecules lie flat on the surface (for example the cluster located inside the circle in Fig. 3b), as noted earlier by Kuchta and and co-workers [39].

Fig. 4 shows the isosteric heat versus loading at 60 K, obtained from the simulations with the 2LJ + 3Q model. The simulation results capture the pattern of the experimental data in the sub-monolayer region, but there are deviations between the simulation results and the experimental data, which we attribute to the difference between the simulation results at 60 K and experimental results for nitrogen adsorption on highly graphitized CarbopackF [37].

#### 3.1.1. $C_2H_4$

Ethylene has a higher quadrupole moment than nitrogen and we therefore expect to see a stronger effect due to the presence of the quadrupole. The simulated isotherm for ethylene adsorption on graphite at 105 K (the bulk triple point) and the experimental data of Menaucourt et al. [40] are shown in Fig. 5.

To improve agreement between experiment and simulation in the

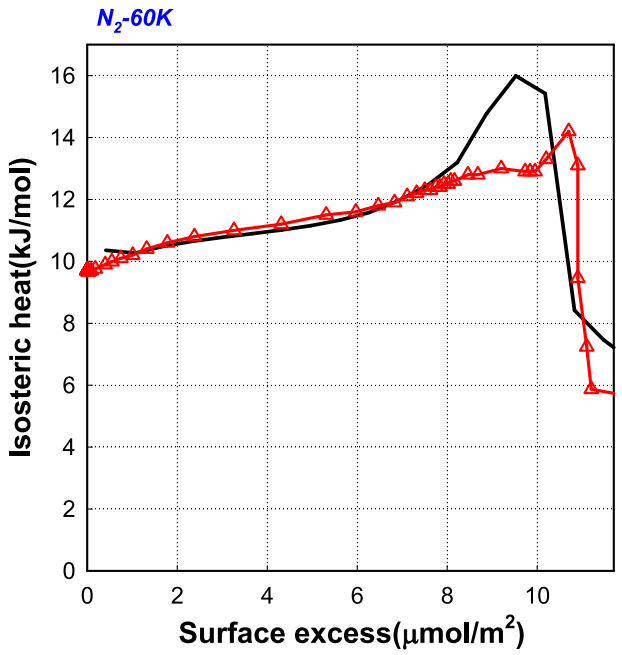


**Fig. 4.** Simulated isosteric heat with the 2LJ + 3Q $N_2$ model (triangle symbols) and experimental data [37] (the solid line) is for nitrogen adsorption at 60 K on graphite.

Henry law region, the cross-molecular parameter between the adsorbate and the adsorbent, computed by the Lorentz-Berthelot rule, was modified to include a binary interaction parameter $k_{sf}$ [41], $\varepsilon_{sf} = (1 - ksf)\sqrt{(\varepsilon_{ss}\varepsilon_{ff})}$, with $k_{sf} = 0.15$ .

The simulated isotherms over the multilayer coverage range for the 2LJ + 4Q model are in better agreement with the experimental data, than those for the LJ model, which supports the argument that the quadrupole moment needs to be included in the description of a non-uniform adsorbed film and affects the adsorbate packing in higher layers.

The distribution of molecules for the 2LJ + 4Q potential model, at $P/P_0 = 0.1$, at which the monolayer is completed, is shown in Fig. 5b as a 3D-plot of density versus distance from the graphite surface and the angle between the molecular axis and the normal vector. The monolayer is about 0.4 nm from the surface and the 90 degree peak in the distribution confirms that most molecules lie flat on the surface with the remaining molecules adopting a vertical orientation, similar to that observed for nitrogen.

Fig. 6a shows the simulated isosteric heats versus loading with the 2LJ + 4Q model together with the component contributions from the adsorbate-adsorbent (SF) interactions and the adsorbate–adsorbate (FF) interactions.

Within the sub-monolayer coverage region (adsorbed density less than 8 μmol/$m^2$), the isosteric heat is greater than the heat of condensation, and is constant across the first-order transition in the first layer which has been discussed in an earlier paper [42]. The importance of the electrostatic terms can be seen in Fig. 6b where the adsorbate–adsorbate contribution is decomposed into LJ and electrostatic contributions. Before the first-order condensation of the first layer occurs, the contribution from the electrostatic interactions to the heat released by the adsorbate–adsorbate interactions is less than 2 kJ/mol, and it increases very sharply to 6 kJ/mol at the completion of the monolayer, as the molecules rearrange and re-orient in the monolayer in order to maximize the quadrupole–quadrupole interactions, with some molecules adopting the vertical orientation seen in the orientation distribution in Fig. 5b.

### 3.1.2. $CO_2$

Simulations using the 1CLJ and 3LJ + 3Q models adsorbed on graphite at 193 K and 273 K, were tested against the data of Beebe et al. [43] and of Guillot and Stoeckli [44]. The 1CLJ model over-predicts the saturation pressure [45] at 193 K, but the simulated adsorption isotherm agrees with the experimental data if plotted against absolute pressure as shown in the inset in Fig. 7a. The simulated isotherms and the experimental data at 193 K show that the adsorbed density at the coexistence pressure $P_0$ is less than twice the statistical monolayer density (incomplete wetting), while those at 273 K, plotted in Fig. 7b, show complete wetting.

Fig. 8 shows the simulated isosteric heats obtained with the 1CLJ and 3LJ + 3Q models together with the experimental data of Spencer et al [43] at 193 K. The 3LJ + 3Q $CO_2$ model fits the experimental data better because the adsorbate–adsorbate interactions (FF) are augmented by the electrostatic contributions which optimise the molecular packing at the completion of the monolayer (around 8 μmol/$m^2$).

From the analysis of the isotherm and the isosteric heat for $N_2$, $C_2H_4$, and $CO_2$ adsorption on graphite we can draw the following general conclusions:

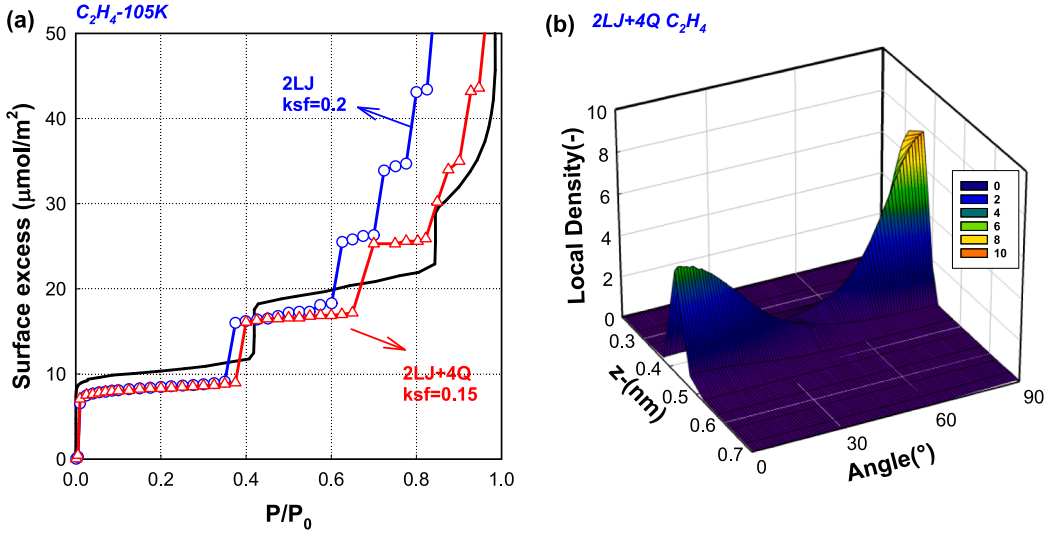


**Fig. 5.** (a) Simulated isotherms with 2LJ and 2LJ + 4Q models for ethylene adsorption at 105 K on graphite. Experimental data is shown as the black solid line. The value of $P_0$ is given in Table 9. (b) Orientation density distribution of the centre of mass at 105 K and 0.1 reduced pressure.

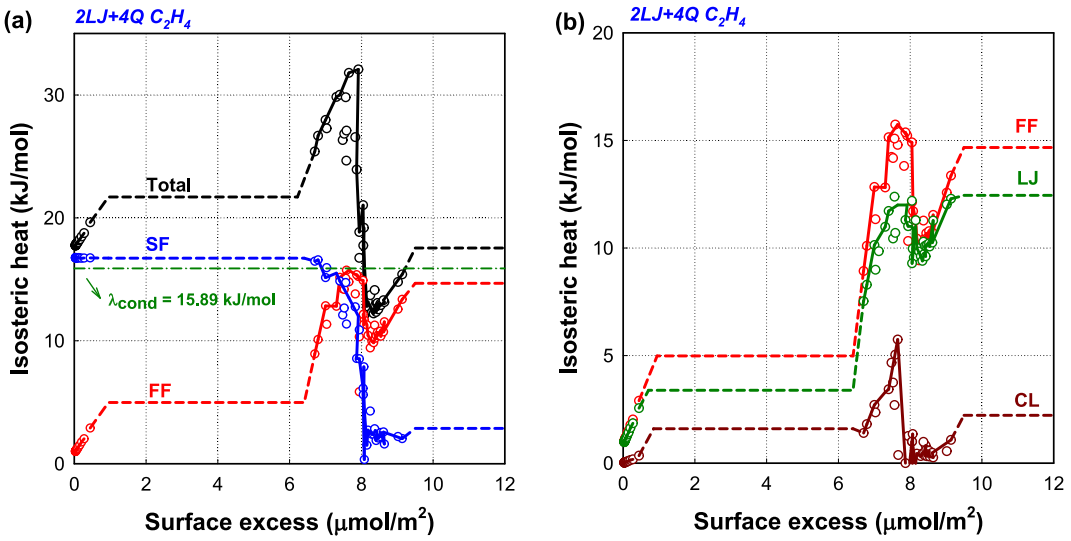


**Fig. 6.** (a) Simulated isosteric heat and contributions from the adsorbate-adsorbent (SF) and adsorbate–adsorbate interactions (FF). (b) The contributions from (LJ) and electrostatic interactions (CL) to the adsorbate–adsorbate contributions (FF) for $C_2H_4$ adsorption on graphite at 105 K.

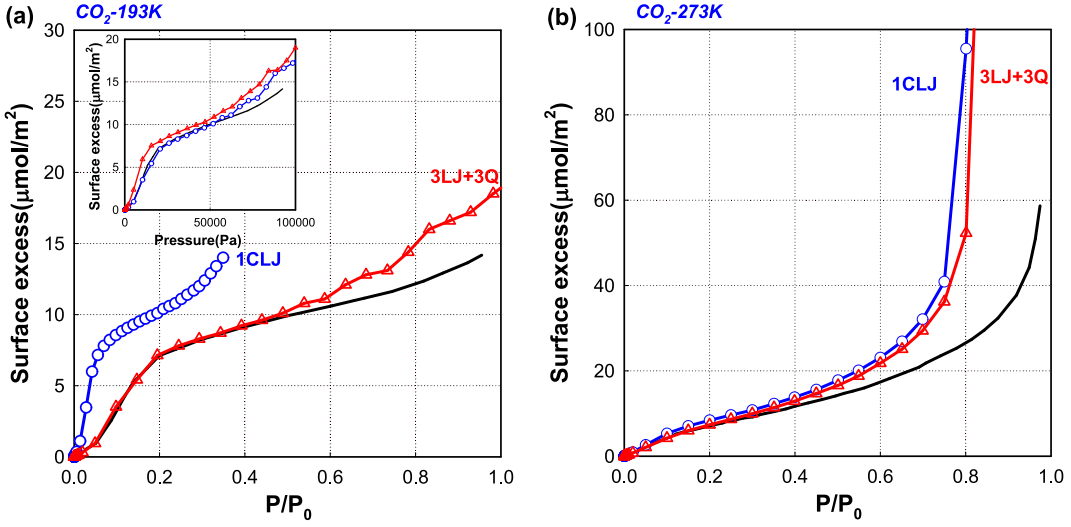


**Fig. 7.** Simulated isotherms with 1CLJ and 3LJ + 3Q models for $CO_2$ adsorption at (a) 193 K and (b) 273 K on graphite with $k_{sf} = 0.05$ and 0.0635 for the 1CLJ model and the 3LJ + 3Q model [41]respectively. The inset figure is the isotherm plotted versus absolute pressure. Experimental data are shown as the black solid line. The value of $P_0$ is given in Table 10.

1. The experimental isotherm and the isosteric heat are better fitted when electrostatic interactions (quadrupolar models) are included in the potential functions.
2. The packing of molecules in the first layer is strongly affected by the quadrupole moment, which has a propagation effect in building higher layers.
3. Most molecules in the first layer on the surface lie flat on the surface, with a few molecules adopting other orientations; for example in the pinwheel structures of nitrogen.

### 3.2. The effects of adsorbate quadrupoles on wetting maps

The quadrupolar potential models for nitrogen, ethylene and carbon dioxide have been used to simulate adsorption on planar substrates of different adsorption strength to construct wetting maps. The choice of saturation pressure, $P_0$, is critical in the construction of a wetting map, and the details of our $P_0$ calculations for the adsorbates in this paper are given in Table 7 to Table 10.

#### 3.2.1. Generic mechanism of wetting behaviour

Using GCMC simulation, we obtained wetting/non-wetting maps, and explored the microscopic origins behind the layering temperature and the wetting temperature for argon, nitrogen, ethylene and carbon dioxide. The common features, shared by all these adsorbates, are shown in the schematic wetting and heat maps in Fig. 9a and 9b, respectively. From these maps we distinguish two adsorbent substrates to exemplify a strong adsorbent ***I***, and a weak adsorbent ***II***, located by the yellow circles in Fig. 9.

The wetting map in Fig. 9a shows regions of non-wetting, incomplete wetting and complete wetting over the space bounded by temperature and adsorbent strength. These regions are separated by three lines: (1) the wetting temperature ($T_W$) line (blue dashed line) separating the wetting and non-wetting regions, (2) the roughening temperature ($T_R$) line (the red dotted line) separating the wetting and incomplete wetting regions and (3) the layering temperature line for the first layer ($T_{L,1}$) (black solid line); separating the incomplete wetting and non-wetting regions. Within the incomplete wetting region, there is a family of layering temperatures for the second and higher layers, with $T_{L,n+1} >$

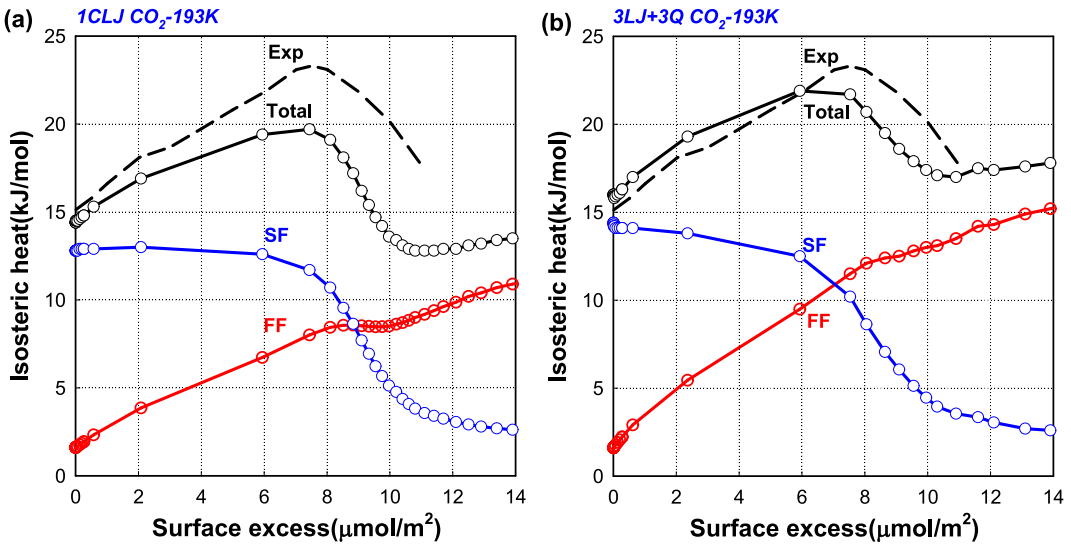


**Fig. 8.** Simulated isosteric heats and the contributions from the adsorbate-adsorbent (SF) and adsorbate–adsorbate (FF) interactions; (a) 1CLJ model and (b) 3LJ + 3Q model for $CO_2$ adsorbed on graphite at 193 K.

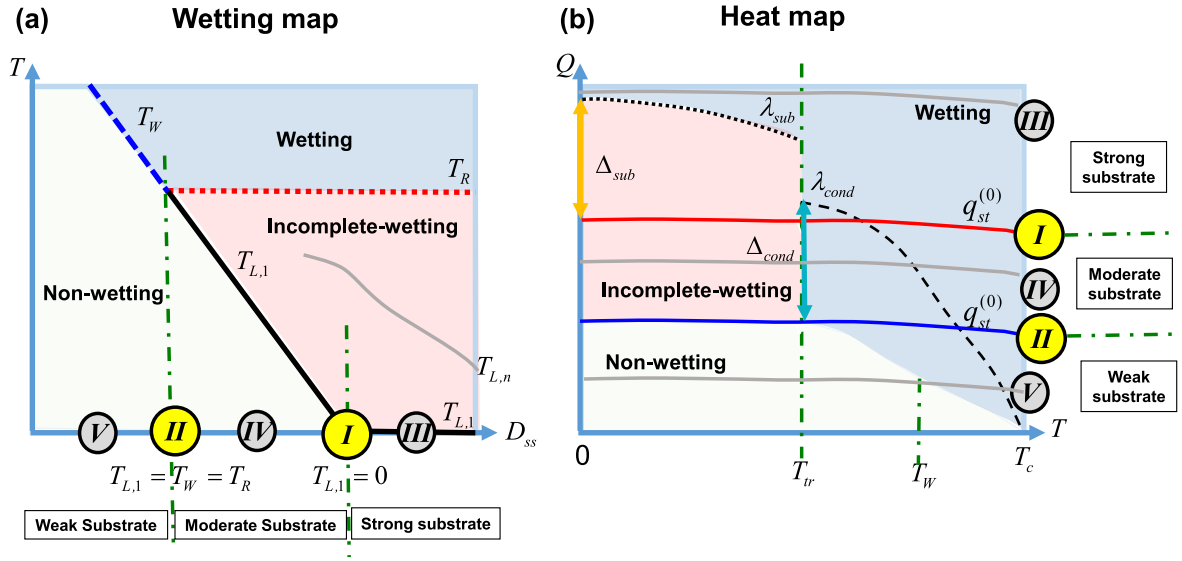


**Fig. 9.** (a) Schematic map showing the separation of non-wetting/incomplete wetting/complete wetting zones in a temperature and surface affinity $D_{ss}$ space. (b) The schematic map for the heat of sublimation (condensation) of fluid molecule and the isosteric heats at zero loading as a function of temperature.

$T_{L,n}$ where $n$ is the layer $n$. From this wetting map, the layering temperature of the first layer for adsorbent ***I***, $T_{L,1}$, is 0 K, with stronger substrates having $T_{L,1} = 0$Kand weaker adsorbents having $T_{L,1} > 0$K. For substrate ***II*** the layering temperature becomes the wetting temperature, which is the same as the roughening temperature.

The schematic map in Fig. 9b shows the heats of sublimation ($\lambda_{sub}$) and condensation ($\lambda_{cond}$) at temperatures above and below the triple point temperature of the bulk phase, and the isosteric heats at zero loading ($q_{st}^{(0)}$) for adsorbates on substrates of various strength as a function of temperature. As the loading is increased the adsorbate configuration contributes to the subsequent adsorption of higher adsorbate layers and therefore plays a part in the wetting/non-wetting behaviour at $P_0$.

To elucidate the distinction between substrates ***I*** and ***II***, we establish the connection between the wetting map and the heat map for these substrates. We define the difference between the isosteric heat at zero loading $q_{st}^{(0)}$and the heat of sublimation or condensation at temperature$T$:

$$\Delta_{sub}(T) = q_{st}^{(0)} - \lambda_{sub}\Delta_{cond}(T) = q_{st}^{(0)} - \lambda_{cond}$$

When either $\Delta_{sub}$ or $\Delta_{cond}$ is positive, incomplete wetting occurs and transition to wetting occurs when the temperature is greater than the roughening temperature.

We denote the energy contributed from the adsorbate–adsorbate interactions during the course of adsorption by $Q_{FF}$.

Substrate ***I*** has a layering temperature $T_{L,1}$ of 0 K in the first layer. Between $T_{L,1}$ and $T_R$ there is incomplete wetting, and complete wetting occurs at temperatures above the roughening temperature. This substrate is at the lower limit of strong adsorbents, and any weaker substrates have a layering temperature greater than 0 K in the first layer, which increases with decreasing affinity.

Fig. 9b shows that at temperatures below the triple point temperature $\Delta_{sub}(T)$is less than 0 because the isosteric heat at zero loading is less than the heat of sublimation. However, the contribution $Q_{FF}$, from the adsorbate–adsorbate interactions is $>\Delta_{sub}(T)$, and therefore the layering temperature for the first layer is 0 K. As the temperature is increased, the

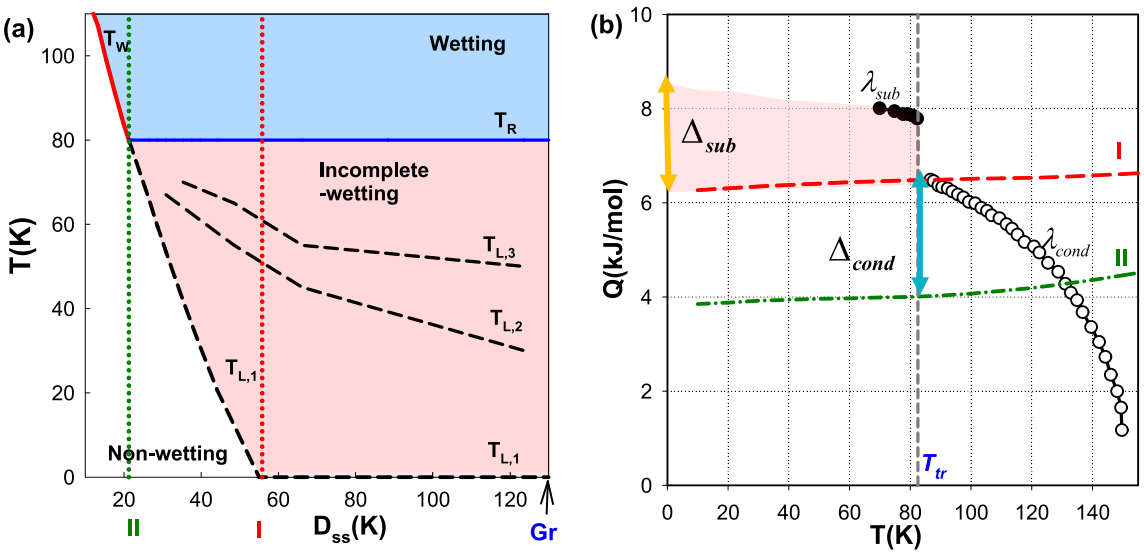


**Fig. 10.** (a) The wetting map in T-$D_{ss}$ space for Ar showing (b) Plots of the heat of sublimation (solid circles) for Ar obtained from simulations of vapour-solid equilibria by Chen et al. [45], the heat of condensation (empty circles) obtained with kMC simulations of vapour-liquid equilibria. [47]. The solid lines show the isosteric heats at zero loading obtained by Monte Carlo integration of the Boltzmann factor [48] for substrates I and II as marked in the wetting map (a).

difference between $\Delta_{sub}(T)$ and $Q_{FF}$ becomes smaller and higher layers are formed sequentially in the incomplete wetting region. When the temperature has reached the triple point temperature (the roughening temperature), complete wetting occurs because the probability of adsorbate separations close to the potential minimum increases as the amplitude of thermal fluctuations increases.

For substrates having a higher affinity than substrate ***I***, the layering temperature of the first layer $T_{L,1}$ is 0 K because the magnitude of $\Delta_{sub}(0) = q_{st}^{(0)} - \lambda_{sub}$ is smaller than $Q_{FF}$, as shown for substrate ***III*** in Fig. 9a. Argon, nitrogen and ethylene adsorption on graphite are examples of Substrate ***III***.

On the other hand, for substrates having weaker affinity than substrate ***I***, the layering temperature for the first layer $T_{L,1}$ is greater than 0 K because $\Delta_{sub}(0)$is negative and is not exceeded by $Q_{FF}$. Therefore the first layer does not form unless the temperature is higher as is the case for substrate ***IV*** in Fig. 9a. Carbon dioxide adsorbed on graphite is an example of substrate ***IV***.

Substrate ***II*** is an example in which the layering temperature of the first layer is the same as the wetting temperature at the roughening temperature. When the first layer is formed, higher layers are also formed because of the high thermal fluctuations; and $T_{L,1} = T_W = T_R = T_{tr}$. The heat maps add further insight to understanding the conditions controlling wetting. Plots of Q against T show that when the temperature has reached the triple point temperature, adsorption on the surface competes with the cohesiveness of the bulk liquid, and that the difference $\Delta_{cond}(T_{tr}) = q_{st}^{(0)} - \lambda_{cond}$ then becomes equal to or greater than $Q_{FF}$ the energy contributed by the adsorbate–adsorbate interactions, resulting in a complete wetting.

For substrates having affinity less than that of substrate ***II***, the wetting temperature is greater than the roughening temperature because the adsorbent strength is too weak to induce wetting unless there is sufficient thermal fluctuation. An example is substrate ***V***.

We next consider the actual wetting maps for the adsorbates examined in this paper. The values of $D_{ss}$(K) for substrates ***I*** and ***II*** are summarized in Table 11.

*3.2.1.1. Argon.* The non-wetting/wetting behaviour of adsorbed argon on planar graphite substrates has been previously studied in detail by Prasetyo et al. [46] using the M−Ar potential model, and their results are summarized here in the wetting map in Fig. 10a. The substrates ***I*** and ***II*** discussed above are also labelled in the wetting and heat maps in Fig. 10a and Fig. 10b.

To further investigate the role of $Q_{FF}$ in the formation of the first layer, we simulated the adsorption of argon adsorption on 10–4-3 graphite at 40 K. At this temperature the isotherm exhibits a first-order transition. Fig. 11a and 11b show the GCMC and kMC isotherms and the isosteric heat curve for argon adsorption on graphite.

Snapshots from the GCMC isotherm during the build-up of the first layer, are shown in Fig. 11c for points A to E marked on the isotherm. The layering process starts with the formation of clusters of molecules (Point A), followed by the coalescence of clusters to form circular 2D-islands (Point B). As more molecules are added the 2D-island becomes a 2D-dense phase with (approximately) linear interfaces separating it from the rarefied phase (point C). Further adsorption occurs at the linear boundaries between the two phases. At this point, $Q_{FF}$ is due to the interaction between the added molecule and molecules at the boundary of the condensed phase, and has a constant value of, $Q_{FF} = 2.2kJ/mol$, shown as a red curve in Fig. 11b.

As adsorption progresses and the number of molecules in the condensed phase become larger, the rarefied phase becomes a monolayer surrounding a 2D-vapour bubble (point D). Finally, the monolayer is completed as a hexagonal packing, as confirmed by the 2D-radial distribution at E (Fig. 11d). The mechanism described here for molecular layering across a *vdW* loop of the canonical isotherm is applicable for the other adsorption systems considered in this paper.

We can now establish a connection between the wetting map and the heat map to explain the mechanisms behind the substrates ***I*** and ***II***

1. Substrate ***I***: At 0 K, complete wetting occurs.
2. Substrate ***II***: At temperatures between 0 K and the triple point temperature, the difference $\Delta_{sub}(T)$ is negative and the system is non-wetting. At the triple point temperature the adsorbate–adsorbate interactions, reach a value of $Q_{FF} = 2.2$kJ/mol which is equal to -$\Delta_{sub}(T)$ , and complete wetting occurs.

*3.2.1.2. $N_2$.* The wetting map and heat map from the simulations of $N_2$ adsorption on planar substrates of various affinities are summarized in Fig. 12a and b. The differences $\Delta_{sub}(T)$and $\Delta_{cond}(T)$, at 0 K and the triple point temperature for the Substrates ***I*** and ***II*** are listed in Table 3. The energy provided by the adsorbate–adsorbate interactions prior to the formation of the first layer, $Q_{FF}$, as 2.6 kJ/mol. Details of this are presented in Fig. 21. Table 3 shows that this energy is > -$\Delta_{sub}$at 0 K for

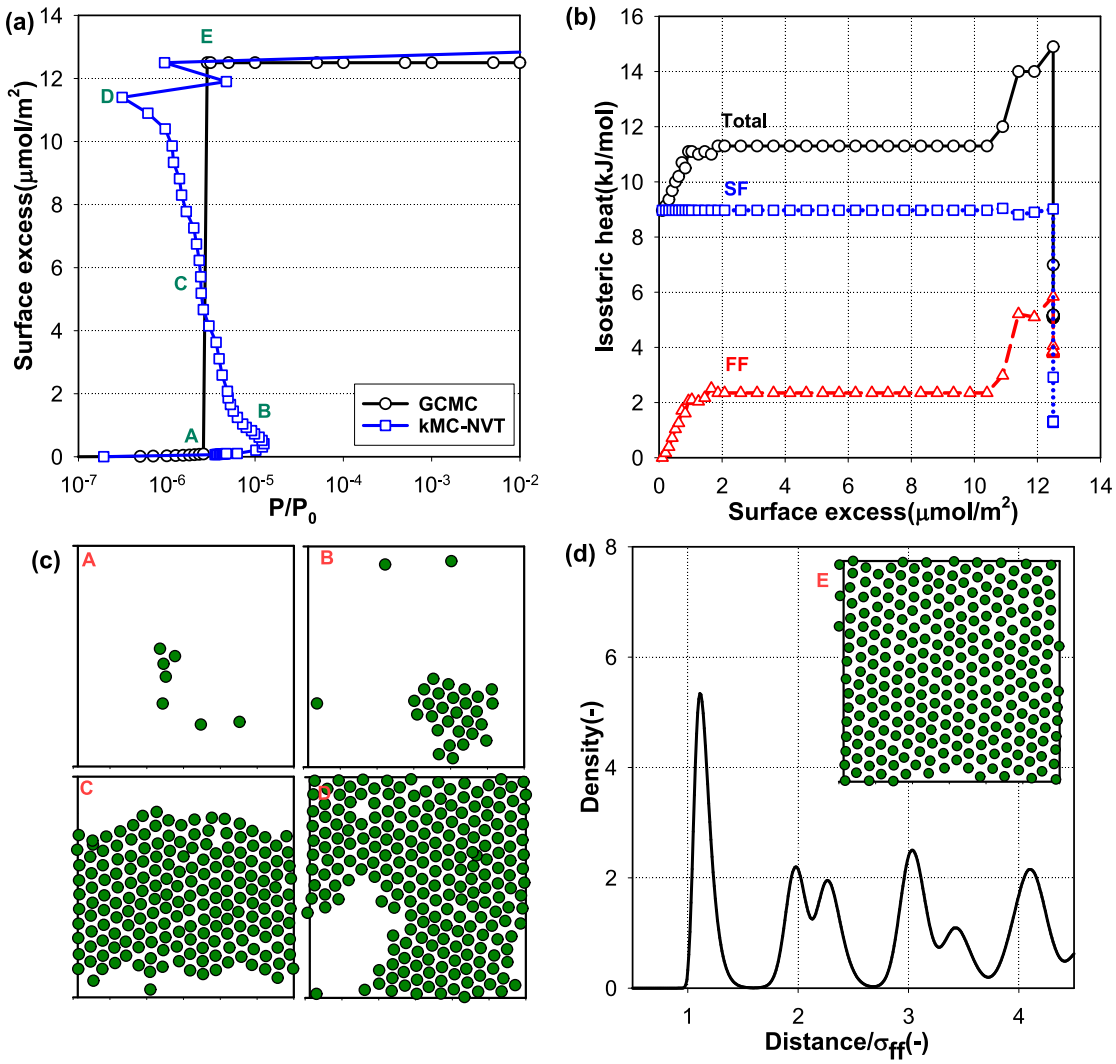


**Fig. 11.** (a) Isotherms for argon adsorption at 40 K on graphite, simulated in GCMC and kMC-NVT ensembles. (b) Isosteric heat and separate contributions from the adsorbate–adsorbate interactions (FF) and the adsorbate-adsorbent interactions (SF) calculated by canonical ensemble simulation [49]. (c) Snapshots of molecules in the first layer at the points marked on the canonical isotherm. (d) 2D radial distribution in the first layer (the inset is the snapshot of molecules for point E).

Substrate ***I*** and therefore the layering temperature of the first layer for this substrate is 0 K. For Substrate ***II***, the energy from the adsorbate-–adsorbate interactions balances $\Delta_{cond}$ at the triple point temperature, and hence $T_{L,1} = T_W = T_R = T_{tr}$ for Substrate ***II***.

*3.2.1.3. $C_2H_4$.* The wetting map and the heat maps for ethylene adsorbed on 10–4-3 graphite are shown in Fig. 13a and b, respectively. Substrates ***I*** to ***II*** are marked in these figures and the details of the isosteric heat versus loading for ethylene adsorption at 50 K are shown in Fig. 21. The energy contributed from the adsorbate–adsorbate interactions in building the first layer, $Q_{FF}$, is 6.3 kJ/mol and was found to be $>-\Delta_{sub}(0)$ for Substrate ***I*** and $-\Delta_{cond}$at the triple point temperature for Substrate ***II*** given in Table 4.

*3.2.1.4. $CO_2$.* Fig. 14a and Fig. 14b show the non-wetting/wetting and heat maps for $CO_2$ adsorption on substrates of different strength with the locations of Substrates ***I*** to ***II*** marked. The values of $\Delta_{sub}(0)$,$\Delta_{cond}(T_{tr})$ in Table 5 show that the adsorbate–adsorbate energy is $> \Delta_{sub}$ or $\Delta_{cond}$ for substrate ***I*** and therefore $T_{L,1} = 0$K. For Substrate ***II***, $T_{L,1} = T_W = T_R = T_{tr}$ since $Q_{FF}$is $> \Delta_{cond}(T_{tr})$. The decomposed heat curves are shown in Fig. 21.

Xu et al. [8], have shown that the bulk triple point temperature separates the incomplete wetting region from the complete wetting region.

*3.2.2. Comparison of wetting maps for adsorbate molecules*

We now consider the effects of electrostatic interactions on the wetting behaviour of the adsorbates on substrates of different strengths. Values of $D^*(Gr)$, defined in Eq. (1), are given in Table 6 and show that $D^*(Gr)$ decreases with increase in the quadrupole strength , suggesting that the strength of the adsorbate-adsorbent interaction is lower as quadrupole strength increases. compared to the intermolecular interactions. For argon and nitrogen, graphite is a stronger adsorbent than ***Substrate II*** because the isosteric heat at zero loading is higher than the heat of sublimation, therefore, the layering temperature for the first layer is 0 K. Ethylene has a stronger quadrupole moment than nitrogen, its affinity for graphite is higher than ***Substrate II;*** therefore the layering temperature of the first layer is 0 K even though the isosteric heat at zero loading is less than the heat of sublimation. Here the difference is made up from the energy provided by the adsorbate–adsorbate interactions. Incomplete wetting occurs for temperatures between 0 K and the roughening temperature of 105 K, which is in agreement with the experimental data of Sutton et al. [51] and Menaucourt et al. [40]. $CO_2$ which has the strongest quadrupole moment of the four adsorbates, graphite falls in the class of moderately strong adsorbents, i.e. between ***Substrate I*** and ***Substrate II*** and the layering temperature for the first

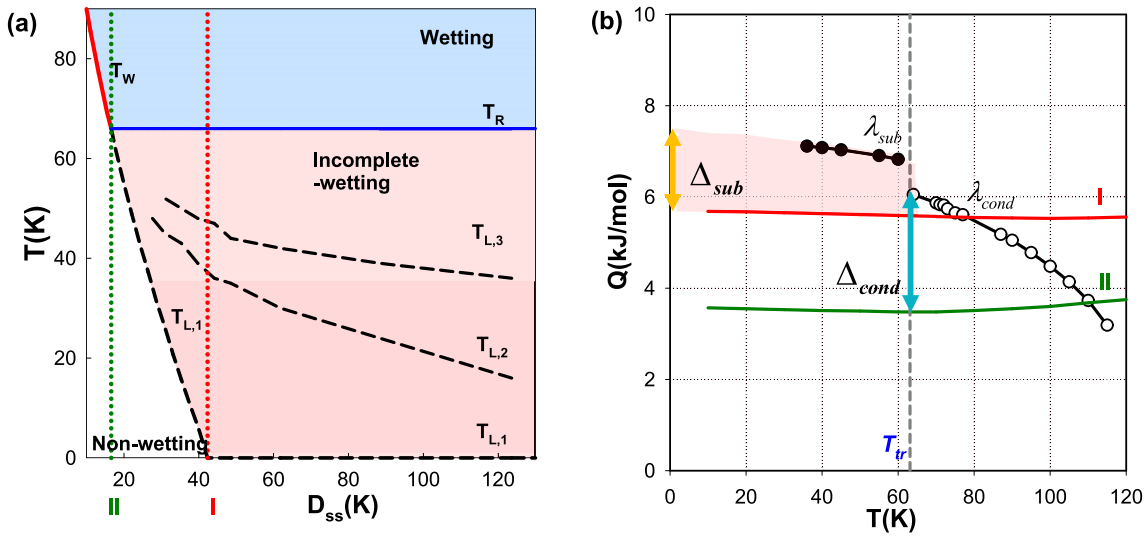


**Fig. 12.** (a) The wetting map for 2LJ + 3Q $N_2$ showing different wetting regions as a function of the temperature and the surface affinity $D_{ss}$. (b) Plots of the heat of sublimation (solid circles) for 2LJ + 3Q $N_2$ from Brown and Ziegler [50], the heat of condensation (empty circles) are from kMC simulations of vapour-liquid equilibria [47]. The solid lines show the isosteric heats at zero loading for substrates of different strength obtained by Monte Carlo integration of the Boltzmann factor [48].

**Table 3**
The difference between the heat of sublimation or condensation and isosteric heat at zero loading for $N_2$ on chosen substrates (**I** and **II**) and its maximum adsorbate–adsorbate interaction energy.

| Substrate | $\Delta_{sub}(0)$(kJ/mol) | $\Delta_{cond}(T_{tr})$(kJ/mol) | $Q_{FF}$(kJ/mol) |
|---|---|---|---|
| **I** | −2.2 | −0.5 | 2.6 |
| **II** | −3.8 | −2.6 | |

layer for graphite was found to be 90 K.

To compare the wetting behaviour of adsorbates that have different intermolecular strengths, as reflected in the triple point and critical temperatures, we define a non-dimensional temperature:

$$\theta = (T - T_{tr})/(T_c - T_{tr})$$

The triple point and critical temperatures for these adsorbates are given in Table 6. The scaled roughening temperature, $\theta_R = (T_R - T_{tr})/(T_c - T_{tr})$ are also shown in the same table.

The parameter $D^*$ (eq. (1)) is the ratio of the strength of the adsorbate-adsorbent interactions to that of the adsorbate–adsorbate interactions for a given adsorbent. To assess the adsorbent strength of a substrate, we take graphite as a reference and define a reduced affinity

**Table 4**
The difference between the heat of sublimation or condensation and isosteric heat at zero loading for $C_2H_4$ on chosen substrates (**I** and **II**) and the maximum adsorbate–adsorbate energy.

| Substrate | $\Delta_{sub}(0)$(kJ/mol) | $\Delta_{cond}(T_{tr})$(kJ/mol) | $Q_{FF}$(kJ/mol) |
|---|---|---|---|
| **I** | −4.3 | −0.24 | 6.3 |
| **II** | −10.0 | −6.20 | |

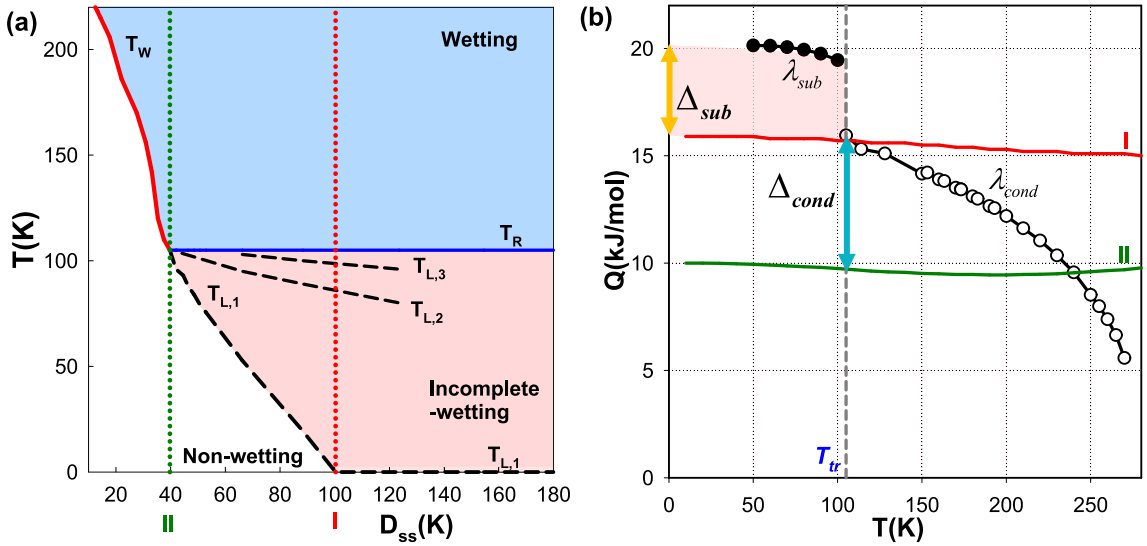


**Fig. 13.** (a) The wetting map for ethylene as a function of temperature and adsorbent strength $D_{ss}$. (b) Plots of the heats of sublimation (solid circles) for 2LJ + 4Q $C_2H_4$ from Brown and Ziegler [50], and the heats of condensation (empty circle) obtained from kMC simulations of VLE [47]. The solid lines show the isosteric heats at zero loading for substrates of different strength obtained by Monte Carlo integration of the Boltzmann factor [48].

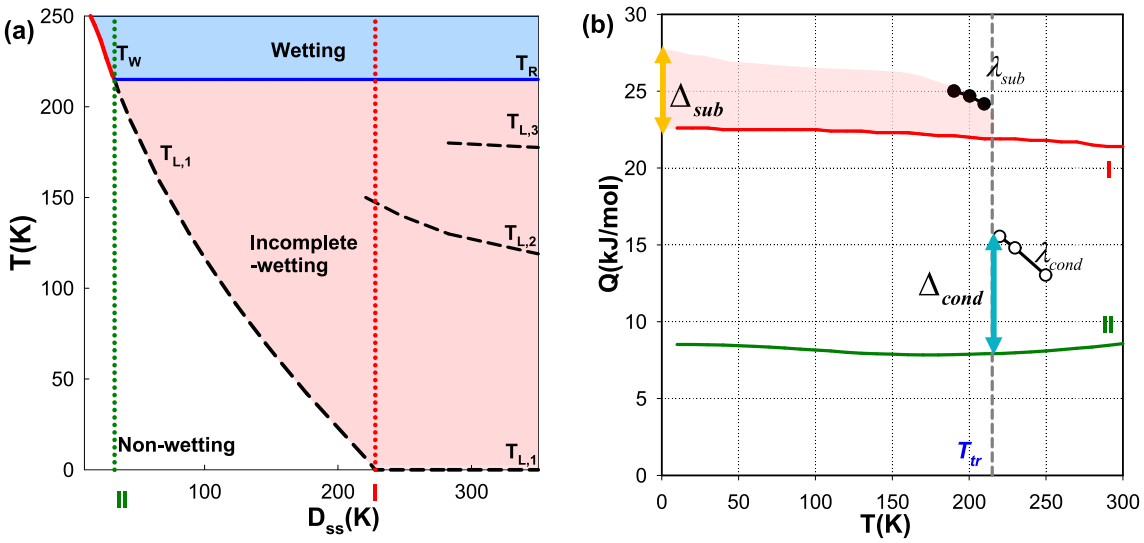


**Fig. 14.** (a) The wetting map for carbon dioxide as a function of the temperature and the adsorbent strength $D_{ss}$. (b) Plots of the heat of sublimation (solid circles) for 3LJ + 3Q $CO_2$ obtained from simulations of vapour-solid equilibria by Chen et al. [45], the heat of condensation (empty circles) obtained from kMC simulations of vapour-liquid equilibria [47]. The solid lines show the isosteric heats at zero loading for substrates of different strength obtained by Monte Carlo integration of the Boltzmann factor [48].

**Table 5**
The difference between the heat of sublimation or condensation and isosteric heat at zero loading for $CO_2$ on chosen substrates (**I** and **II**) and its maximum adsorbate–adsorbate interaction energy.

| Substrate | $\Delta_{sub}(0)$(kJ/mol) | $\Delta_{cond}(T_{tr})$(kJ/mol) | $Q_{FF}$(kJ/mol) |
|---|---|---|---|
| **I** | −4.3 | 6.12 | 8.1 |
| **II** | −18.5 | −7.8 | |

**Table 6**
Physical properties of the linear adsorbates (the units of the quadrupole moment are $10^{-40}$ C $m^2$).

| *Fluid* | *Quadrupole moment* | $T_{tr}/(K)$ | $T_C/(K)$ | $D^*(Gr)$ | $T_R/(K)$ | $\theta_R$ |
|---|---|---|---|---|---|---|
| Ar | 0 | 82.5 [45] | 154.5 [45] | 9.0 | 80 | −0.04 |
| $N_2$ | −4.7 | 63 | 126.5 [31] | 8.5 | 66 | 0.05 |
| $C_2H_4$ | 6.7 | 104 | 286.3 [32] | 4.6 | 105 | 0.01 |
| $CO_2$ | −12.2 | 212 [45] | 306.8 [45] | 3.3 | 215 | 0.03 |

**Table 7**
Summary of $P_0$ of M−Ar at different temperature used in our simulations.

| Temperature (K) | $P_0$(Pa)for M−Ar |
|---|---|
| 40 | $2.04 \times 10^0$ |

**Table 8**
Summary of $P_0$ of nitrogen for different temperature used in simulations.

| Temperature (K) | $P_0$(Pa)for Exp | $P_0$(Pa)for 1CLJ | $P_0$(Pa)for 2LJ + 3Q |
|---|---|---|---|
| 60 | $5.94 \times 10^3$ | $6.40 \times 10^3$ | $6.20 \times 10^3$ |
| 77 | $9.31 \times 10^4$ | $9.13 \times 10^4$ | $9.50 \times 10^4$ |

$$\Omega = \frac{D^*}{D^*(Gr)}$$

The wetting maps reconstructed in a reduced temperature θ reduced affinity space are shown in Fig. 15.

For a given reduced temperature $\theta_1$ as marked in Fig. 15, we see that non-wetting is expected for all adsorbates on very weak substrates (less than A). As the affinity of the substrate increases complete wetting occurs for argon and nitrogen for substrates with affinities between A and B but ethylene and carbon dioxide are non-wetting, due to the effects of

**Table 9**
Summary of $P_0$ for ethylene for temperature used in simulations.

| Temperature (K) | $P_0$(Pa)for Exp | $P_0$(Pa)for 2LJ | $P_0$(Pa)for 2LJ + 4Q |
|---|---|---|---|
| 105 | $1.46 \times 10^2$ | $4.86 \times 10^2$ | $1.45 \times 10^2$ |

**Table 10**
Summary of $P_0$ of carbon dioxide (3LJ + 3Q model) for the different temperatures used in this paper.

| Temperature (K) | $P_0$(Pa)for Exp | $P_0$(Pa)for 1CLJ | $P_0$(Pa)for 3LJ + 3Q |
|---|---|---|---|
| 193 | $9.67 \times 10^4$ | $3.72 \times 10^5$ | $1.06 \times 10^5$ |
| 273 | $3.48 \times 10^6$ | $3.53 \times 10^6$ | $3.50 \times 10^6$ |

**Table 11**
Strength of the substrate ($D_{ss}$(K)for Ar, $N_2$, $C_2H_4$ and $CO_2$ on substrates I and II.

| Substrate | adsorbate molecule | | | |
|---|---|---|---|---|
| | Ar | $N_2$ | $C_2H_4$ | $CO_2$ |
| **I** | 55.8 | 42.4 | 100.3 | 227.95 |
| **II** | 21.3 | 16.6 | 39.7 | 32.54 |

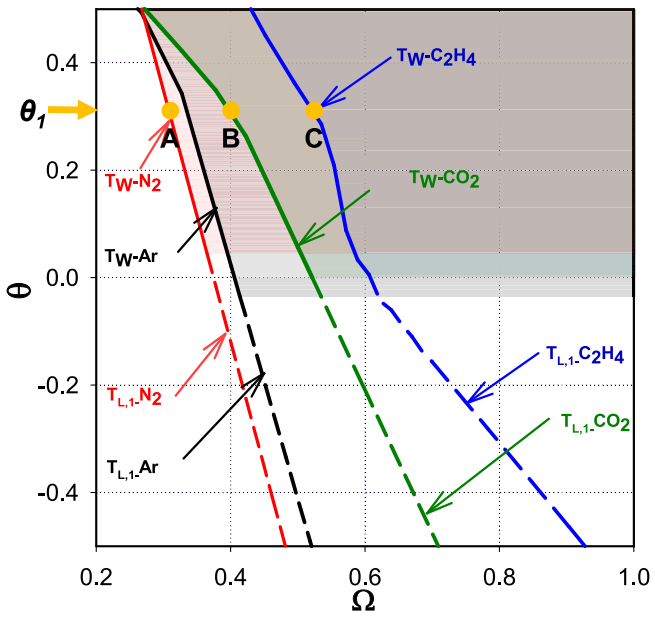


**Fig. 15.** Wetting maps of argon, nitrogen, ethylene and carbon dioxide in terms of the reduced temperature and Ω.

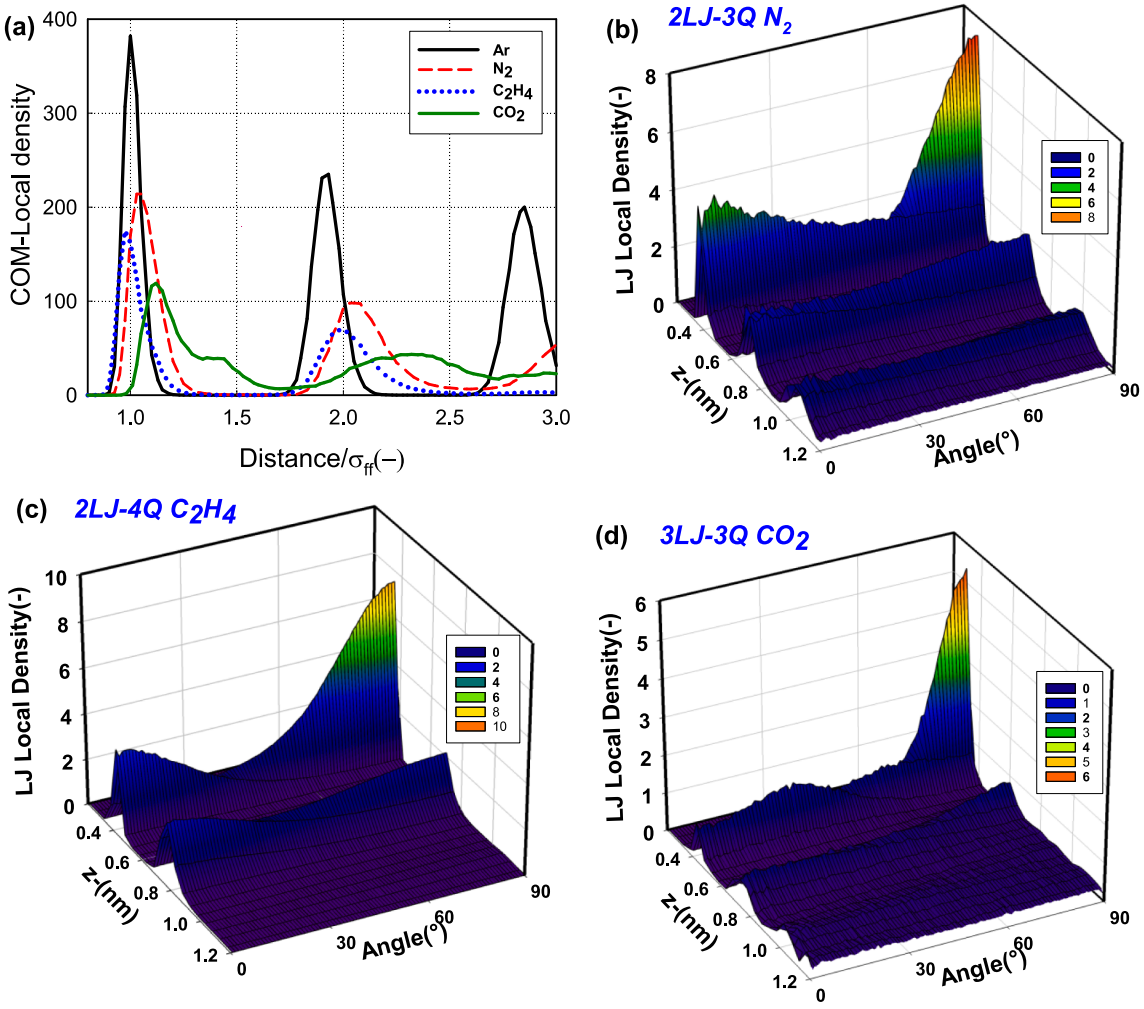


**Fig. 16.** (a) Local density distribution of the centre of mass of M−Ar at 83 K, 2LJ + 3Q $N_2$ at 77 K, 2LJ + 4Q $C_2H_4$, at 116 K and 3LJ + 3Q $CO_2$ at 215 K at $P_0$ versus distance away from the graphite surface. 3D plots of orientation density distributions of (b) 2LJ + 3Q $N_2$ at 77 K, (c) 2LJ + 4Q $C_2H_4$, at 116 K and (d) 3LJ + 3Q $CO_2$ at 215 K at $P_0$ on a graphite surface.

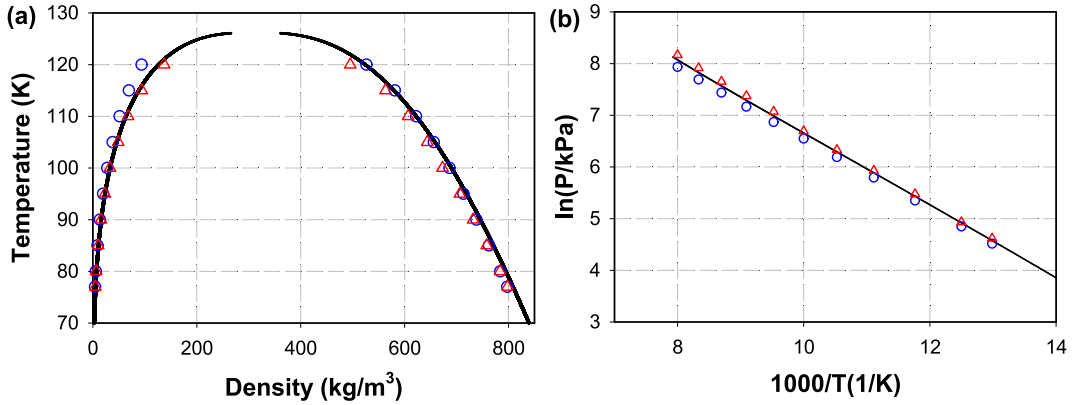


**Fig. 17.** (a) The vapour-liquid coexistence curve for $N_2$. (b) Logarithm of the saturated vapour pressure versus the inverse of temperature for $N_2$. Experimental data are shown as the solid line and the simulation results from the 2LJ + 3Q $N_2$ model and the 1CLJ $N_2$ model are shown as triangles and circles, respectively.

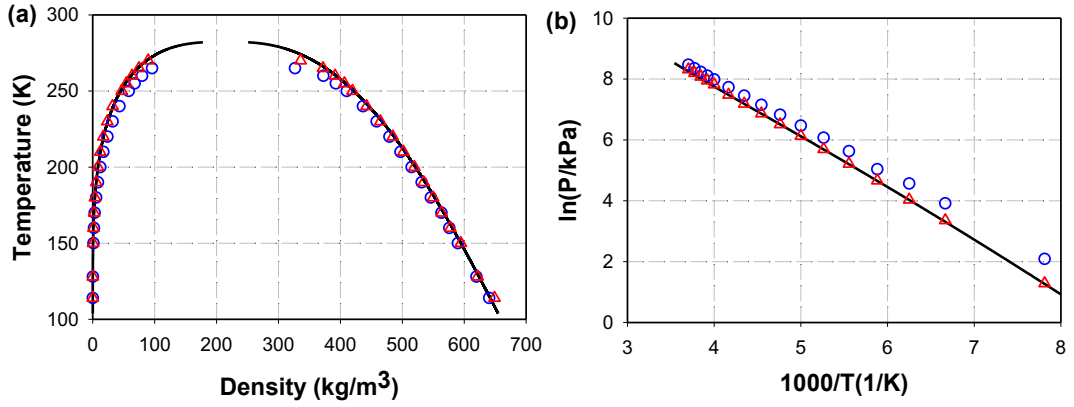


**Fig. 18.** (a) The vapour-liquid coexistence curve for $C_2H_4$. (b) Logarithm of the saturated vapour pressure versus the inverse of temperature for $C_2H_4$. Experimental data are shown as solid lines and the simulation results for the 2LJ + 4Q $C_2H_4$ model and the 2LJ $C_2H_4$ model are shown as the triangles and circles, respectively.

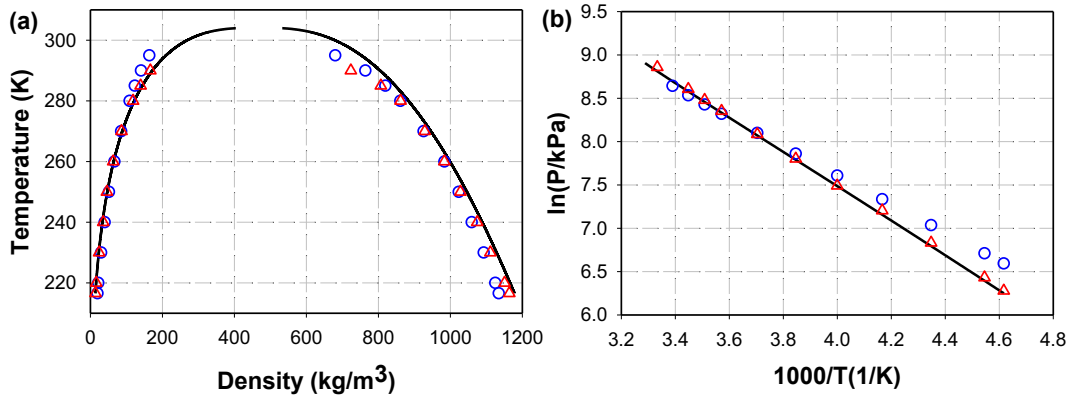


**Fig. 19.** (a) The vapour-liquid coexistence curve for $CO_2$. (b) Logarithm of the saturated vapour pressure versus the inverse of temperature for $CO_2$. Experimental data are shown as solid lines and the simulation results from the 3LJ + 3Q $CO_2$ model and the 1CLJ $CO_2$ model are shown as triangles and circles, respectively.

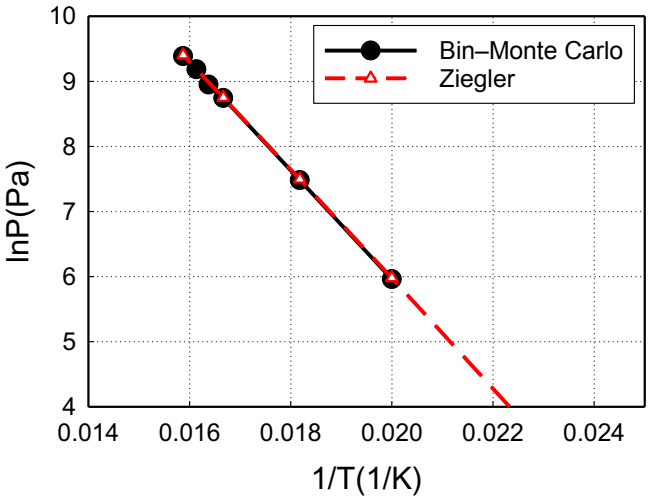


**Fig. 20.** Logarithm of the sublimation pressure versus the inverse of temperature for $N_2$. The values calculated from empirical expressions for sublimation pressure [50] are shown as a dashed line with triangles and the simulation results for the 2LJ + 3Q $N_2$ model with Bin-Monte Carlo [54] are shown as a solid line with circles.

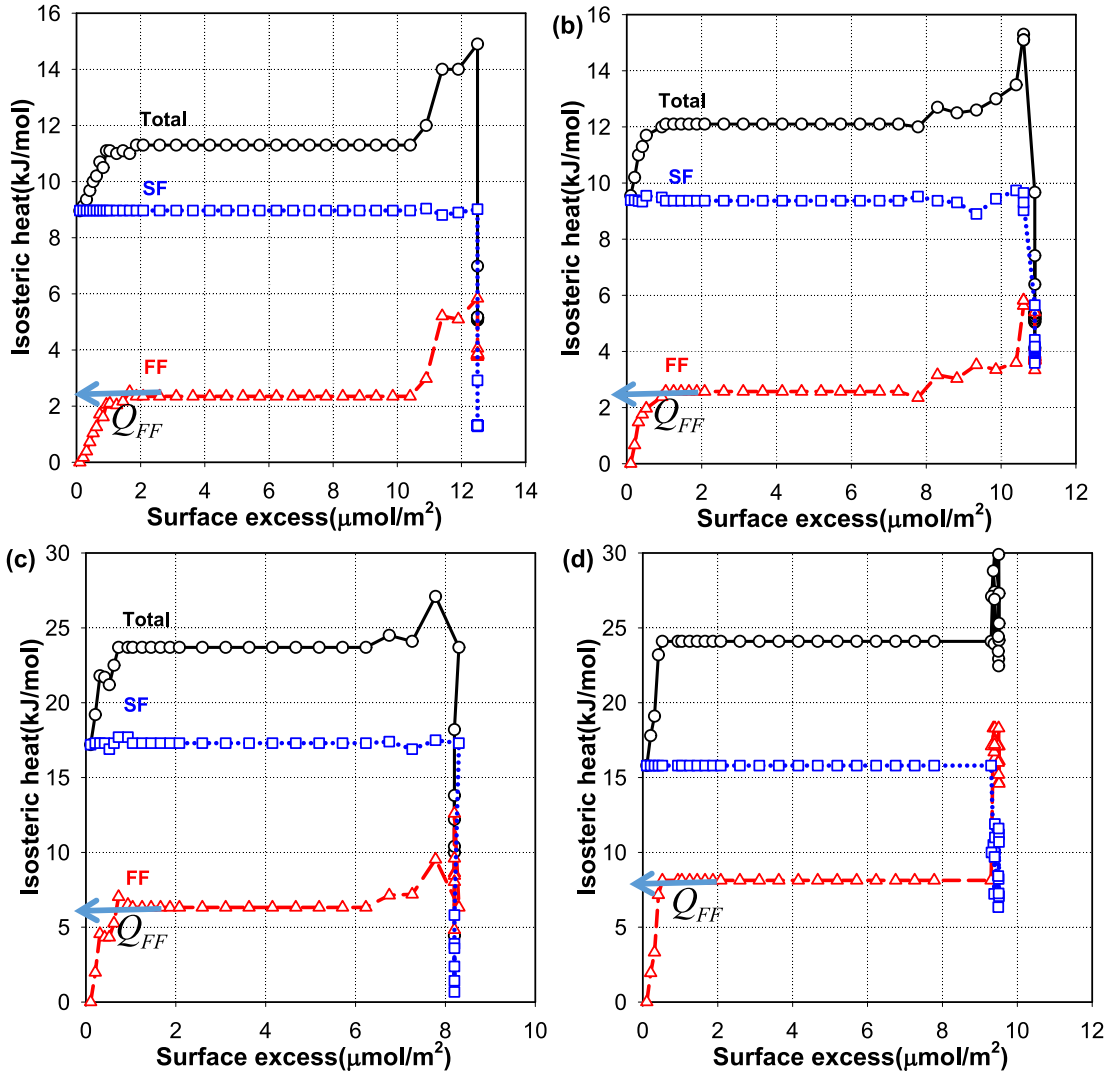


**Fig. 21.** Isosteric heat of adsorption of (a)argon at 40 K, (b) nitrogen at 20 K,(c) ethylene at 50 K and carbon dioxide at 90 K on graphite surface and its contributions from the Fluid- Fluid (FF) and Solid-Fluid (SF) interactions to the first layer. The plateau of the fluid–fluid contribution is the adsorbate–adsorbate interaction energy provided to build the first layer,$Q_{FF}$.

the quadrupoles as discussed earlier. When the affinity is greater than C, wetting occurs for all adsorbates.

The local density distributions for argon, nitrogen, ethylene and carbon dioxide adsorption on graphite at their respective bulk coexistence pressures and roughening temperatures are plotted in Fig. 16a as a function of the distance between the solid and the centre of the fluid molecule. For argon, the peaks are sharp, with clear separation between molecular layers. On the other hand, the first peaks for nitrogen, ethylene and carbon dioxide are broader with a shoulder, indicating of some molecules have vertical orientations. The 3D-orientation density distributions plots for nitrogen, ethylene and carbon dioxide in Fig. 16b, c, d, respectively confirm this structure. Most molecules adopt orientations parallel to the surface to maximize their LJ interactions with graphite. This orientation with respect to the surface is common for all linear adsorbates on graphite at low temperatures [8,37,52] and in carbon pores [34], as confirmed with the analysis of heat of adsorption by Hoory and Prausnitz [53].

## 4. Conclusions

The simulations reported in this paper have address three issues, relating to the wetting on a planar substrates. First, simulations with potential models accounting for the presence of a quadrupole moment give a good account of both vapour-liquid equilibria and adsorption. Secondly, models which include electrostatic interactions have the same characteristics of non-wetting, incomplete wetting and complete wetting, and are governed by the difference between the isosteric heat at zero loading for adsorption on planar substrates and the heats of sublimation and condensation of the bulk fluid. Finally, it was found that most quadrupolar molecules adopt orientations parallel to the surface to maximize their interactions with graphite.

## Declaration of Competing Interest

The authors declare that they have no known competing financial interests or personal relationships that could have appeared to influence the work reported in this paper.

## Acknowledgement

This work is supported by the Australian Research Council (DP160103540). The author Hui Xu gratefully appreciates the financial support from China Scholarship Council and K.P. acknowledges the financial support from the Thailand Research Fund (TRF) via the Royal Golden Jubilee (RGJ) Ph.D. scholarship, batch number 17 (PHD/0156/2557).

## Appendix A

The surface excess density in the system, Γ is defined as

$$\Gamma = \frac{\langle N \rangle - V_{acc}\rho_b}{S}$$

where $\langle N \rangle$ is the ensemble average of the number particles in the system, $V_{acc}$is the accessible volume, where solid–fluid potential is non-positive, $\rho_b$is the density of the bulk gas,$S$ is the surface area of the solid.

The isosteric heat, $q_{st}$, is calculated from the following equation :

$$q_{st} = \frac{\langle N_b \rangle}{f(N_b, N_b)} k_B T - \frac{f(U,N)}{f(N,N) - (V_{acc}/V_b) f(N_b, N_b)}$$

where $N_b$ is the number of molecules occupying the accessible volume of the system at the same density as the bulk phase, $N$ is the number of molecules in the system, $V_{acc}$ is the accessible volume within which the solid–fluid potential energy is non-positive, $V_b$ is the volume that used to simulate the bulk gas phase, $U$ is the configurational energy of the system,$f(X, Y)$ is the fluctuation variable, defined as $f(X, Y) = \langle XY \rangle - \langle X \rangle \langle Y \rangle$, and $\langle \cdot \rangle$ denotes an ensemble average.

The orientation of a fluid molecule is defined as the angle, θ, between the linear molecular axis and the normal vector through the graphite surface. The orientational density distribution was calculated as:

$$\rho(z, \theta) = \frac{\langle N_{z,\theta} \rangle}{L_x L_y \Delta z (sin\theta) \Delta\theta}$$

where $\langle N_{z,\theta} \rangle$ is the average number of molecules in the region bounded by $[z, z + \Delta z]$ and angles are bounded by $[\theta, \theta + \Delta\theta]$.

The local density in the distance of the centre of mas of adsorbate molecules from the surface was calculated as:

$$\rho(z) = \frac{\langle \Delta N_{z,z+\Delta z} \rangle}{L_x L_y \Delta z}$$

where $\langle N_{z,z+\Delta z} \rangle$ is the average number of molecules whose centre of mass in the region bounded by $[z, z + \Delta z]$.

## 6 Appendix B. Physical properties

### 6.1. Vapour-liquid equilibrium

Fig. 17 to Fig. 19 show the performance of the various potential models for the description of the vapour-liquid equilibria (VLE) as plots of the temperature versus the coexistence densities and the vapour pressure as a function of temperature for $N_2$, $C_2H_4$ and $CO_2$. These simulation results were obtained with kMC simulations. It is seen that the multi-site models with fixed partial charges yield a better description of the phase diagram and the vapour pressure than the models with only LJ potentials, indicating that molecular shape and the electrostatic contributions to the potential are significant.

### 6.2. Bulk coexistence pressure

#### 6.2.1. Ar

For argon, the bulk coexistence pressure, $P_0$ was determined from kMC vapour-liquid simulations [47]. At temperatures above and below the triple point temperature, we used the simulation results for vapour-solid equilibrium by Chen et al. [45].

#### 6.2.2. $N_2$

For the 2LJ + 3Q potential model for $N_2$ potential, the bulk coexistence pressure, $P_0$, was determined from kMC simulations of the vapour-liquid equilibria [47] at temperatures above the bulk triple point temperature, $T_{Tr}$. Values of $P_0$ at temperatures below $T_{Tr}$ were taken from experimental data [50] since these are in excellent agreement with the simulation results of vapour-solid equilibria [54] as confirmed by the plots given in Fig. 20.

#### 6.2.3. $C_2H_4$

With the 2LJ + 4Q potential model for $C_2H_4$, we obtained the coexistence pressure of the bulk phase, $P_0$, from kMC simulations of vapour-liquid equilibria (VLE) [47] at temperatures greater than the triple point temperature. , Below the triple point temperature we used the results from Smukala et al. [55]. The experimental data are taken from the NIST [56].

#### 6.2.4. $CO_2$

The coexistence pressure of the bulk phase, $P_0$, was determined from kMC simulations of vapour-liquid equilibrium [47] at temperatures above the triple point temperature. Below the triple point temperature we used the simulation results for vapour-solid equilibrium from Chen et al. [45]. The experimental data were taken from the NIST [56].

## References


[1] D.M. Zhu, J.G. Dash, Surface melting and roughening of adsorbed argon films, Phys. Rev. Lett. 57 (23) (1986) 2959–2962.
[2] Youn, H. S.; Hess, G. B., Reentrant first-order layering transitions in multilayer argon films on graphite. Phys Rev Lett 1990, 64 (8), 918-921.
[3] M. Bienfait, J.L. Seguin, J. Suzanne, E. Lerner, J. Krim, J.G. Dash, Complete and incomplete wetting of krypton and oxygen on graphite: Reentrant type-2 growth on a scale of substrate strength, Phys. Rev. B 29 (2) (1984) 983–987.
[4] U.G. Volkmann, K. Knorr, Ellipsometric study of krypton physisorbed on graphite, Surf. Sci. 221 (1) (1989) 379–393.
[5] G. Quentel, J.M. Rickard, R. Kern, Étude de l'adsorption par ellipsométrie: adsorption du Xe/(0001) graphite, Surf. Sci. 50 (2) (1975) 343–359.
[6] U. Volkmann, K. Knorr, Multilayer growth and wetting behavior of nitrogen physisorbed on graphite, Physical Review Letters 66 (4) (1991) 473–476.
[7] M. Drir, H.S. Nham, G.B. Hess, Multilayer adsorption and wetting: Ethylene on graphite, Phys. Rev. B 33 (7) (1986) 5145–5148.
[8] H. Xu, Y. Zeng, D.D. Do, D. Nicholson, On the Nonwetting/Wetting Behavior of Carbon Dioxide on Graphite, J. Phys. Chem. C 123 (14) (2019) 9112–9120.
[9] X. Zhao, Wetting transition of water on graphite: Monte Carlo simulations, Phys. Rev. B 76 (4) (2007), 041402.
[10] S.R. Friedman, M. Khalil, P. Taborek, Wetting transition in water, Phys Rev Lett 111 (22) (2013), 226101.
[11] Q.K. Loi, L. Prasetyo, S. Tan, D.D. Do, D. Nicholson, Nonwetting/Prewetting/Wetting Transition of Ammonia on Graphite, Langmuir 35 (3) (2019) 641–652.
[12] U.G. Volkmann, H. Mannebach, K. Knorr, Ellipsometric Study of Multilayer Growth and Wetting of $C_2Cl_2F_4$ Physisorbed on Graphite, Langmuir 14 (17) (1998) 4904–4907.
[13] K. Madih-Ayadi, S. Rakotozafy, T. Ceva, B. Croset, N. Dupont-Pavlovsky, P. Convert, I. Mirebeau, E. Ressouche, Growth mode of dichloromethane physisorbed on graphite.: Thermodynamic and structural characterizations, Surf. Sci. 436 (1) (1999) 99–106.
[14] S.M. Gatica, M.W. Cole, To Wet or Not to Wet: That Is the Question, J. Low Temp. Phys. 157 (3–4) (2009) 111–136.
[15] W.A. Steele, in: Chapter Eight - Wetting Phenomena, Elsevier:, Amsterdam, 2008, pp. 167–185.
[16] R. Pandit, M. Schick, M. Wortis, Systematics of multilayer adsorption phenomena on attractive substrates, Phys. Rev. B 26 (9) (1982) 5112–5140.
[17] P.G. De Gennes, Wetting: statics and dynamics, Rev. Mod. Phys. 57 (3) (1985) 827–863.
[18] M.S. Sellers, J.R. Errington, Influence of Substrate Strength on Wetting Behavior, J. Phys. Chem. C 112 (33) (2008) 12905–12913.
[19] W.F. Saam, Wetting, Capillary Condensation and More, J. Low Temp. Phys. 157 (3–4) (2009) 77–100.
[20] H. Ulbricht, R. Zacharia, N. Cindir, T. Hertel, Thermal desorption of gases and solvents from graphite and carbon nanotube surfaces, Carbon 44 (14) (2006) 2931–2942.
[21] A. Terlain, Y. Larher, Phase diagrams of films of linear molecules with large quadrupole moments ($CO_2$, $N_2O$, $C_2N_2$) adsorbed on graphite, Surf. Sci. 125 (1) (1983) 304–311.
[22] M.R. Battaglia, A.D. Buckingham, D. Neumark, R.K. Pierens, J.H. Williams, The quadrupole moments of carbon dioxide and carbon disulphide, Mol. Phys. 43 (5) (1981) 1015–1020.
[23] A. Buckingham, R.-L. Disch, D. Dunmur, Quadrupole moments of some simple molecules, J. Am. Chem. Soc. 90 (12) (1968) 3104–3107.
[24] J.G. Dash, Clustering and percolation transitions in helium and other thin films, Phys. Rev. B 15 (6) (1977) 3136–3146.
[25] Venables, J. A.; Spiller, G. D. T., Nucleation and Growth of Thin Films. In Surface Mobilities on Solid Materials: Fundamental Concepts and Applications, Binh, V. T., Ed. Springer US: Boston, MA, 1983; pp 341-404.
[26] S.J. Tan, L. Prasetyo, Y. Zeng, D. Do, D. Nicholson, On the consistency of NVT, NPT, μVT and Gibbs ensembles in the framework of kinetic Monte Carlo-Fluid phase equilibria and adsorption of pure component systems, Chem. Eng. J. 316 (2017) 243–254.
[27] V.T. Nguyen, S.J. Tan, D. Do, D. Nicholson, Application of kinetic Monte Carlo method to the vapour–liquid equilibria of associating fluids and their mixtures, Mol. Simul. 42 (8) (2016) 642–654.
[28] C. Fan, D. Do, D. Nicholson, E. Ustinov, A novel application of kinetic Monte Carlo method in the description of $N_2$ vapour–liquid equilibria and adsorption, Chem. Eng. Sci. 90 (2013) 161–169.
[29] A. Michels, H. Wijker, H.k. Wijker, Isotherms of argon between 0 C and 150 C and pressures up to 2900 atmospheres, Physica 15 (7) (1949) 627–633.
[30] P.I. Ravikovitch, A. Vishnyakov, R. Russo, A.V. Neimark, Unified approach to pore size characterization of microporous carbonaceous materials from $N_2$, Ar, and $CO_2$ adsorption isotherms, Langmuir 16 (5) (2000) 2311–2320.
[31] J.J. Potoff, J.I. Siepmann, Vapor–liquid equilibria of mixtures containing alkanes, carbon dioxide, and nitrogen, AIChE J. 47 (2001) 1676–1682.
[32] C.D. Wick, M.G. Martin, J.I. Siepmann, Transferable potentials for phase equilibria. 4. United-atom description of linear and branched alkenes and alkylbenzenes, J. Phys. Chem. B 104 (33) (2000) 8008–8016.
[33] M.S. Shah, J.I. Siepmann, M. Tsapatsis, Transferable potentials for phase equilibria. Improved united-atom description of ethane and ethylene, AIChE J. 63 (11) (2017) 5098–5110.
[34] D.D. Do, H.D. Do, Adsorption of Ethylene on Graphitized Thermal Carbon Black and in Slit Pores: A Computer Simulation Study, Langmuir 20 (17) (2004) 7103–7116.
[35] A. Vishnyakov, P.I. Ravikovitch, A.V. Neimark, Molecular level models for CO2 sorption in nanopores, Langmuir 15 (25) (1999) 8736–8742.
[36] W.A. Steele, The physical interaction of gases with crystalline solids: I. Gas-solid energies and properties of isolated adsorbed atoms, Surf. Sci. 36 (1) (1973) 317–352.
[37] C. Fan, D.D. Do, D. Nicholson, J. Jagiello, J. Kenvin, M. Puzan, Monte Carlo simulation and experimental studies on the low temperature characterization of nitrogen adsorption on graphite, Carbon 52 (2013) 158–170.
[38] M. Golebiowska, L. Firlej, B. Kuchta, R. Fabianski, Structural transformations of nitrogen adsorbed on graphite: Monte Carlo studies of spatial heterogeneity in multilayer system, J Chem Phys 130 (20) (2009) 204703, https://doi.org/10.1063/1.3142529.
[39] B. Kuchta, R.D. Etters, Calculated properties of monolayer and multilayer $N_2$ on graphite, Physical review. B, Condensed matter 36 (6) (1987) 3400–3406.
[40] J. Menaucourt A. Thomy X. Duval Variation in temperature function of the number of adsorbed ethylene layers on the cleavage faces of graphite Journal de Physique Colloques 38 C4 1977 pp. C4–195 - C4–200.
[41] D.D. Do, H.D. Do, Effects of potential models on the adsorption of carbon dioxide on graphitized thermal carbon black: GCMC computer simulations, Colloids Surf., A 277 (1-3) (2006) 239–248.
[42] C.Y. Fan, D.D. Do, D. Nicholson, Bin-Monte Carlo simulation of ethylene coexistence and of ethylene adsorption on graphite, Colloid Surf. A-Physicochem. Eng. Asp. 437 (2013) 42–55.
[43] W. Spencer, C. Amberg, R. Beebe, Further studies of adsorption on graphitized carbon blacks, J. Chem. Phys. 62 (6) (1958) 719–723.

[44] A. Guillot, F. Stoeckli, Reference isotherm for high pressure adsorption of $CO_2$ by carbons at 273 K, Carbon 39 (13) (2001) 2059–2064.
[45] B. Chen, J.I. Siepmann, M.L. Klein, Direct Gibbs Ensemble Monte Carlo Simulations for Solid− Vapor Phase Equilibria: Applications to Lennard− Jonesium and Carbon Dioxide, J. Phys. Chem. B 105 (40) (2001) 9840–9848.
[46] L. Prasetyo, Q.K. Loi, S.J. Tan, D.D. Do, D. Nicholson, Effects of temperature on the transition from clustering to layering for argon adsorption on substrates of different strength - Parametric map of wetting, pre-wetting and non-wetting, Microporous Mesoporous Mater (2018).
[47] S.J. Tan, D. Nicholson, D.D. Do, An efficient kinetic Monte Carlo scheme for computing helmholtz free energy and entropy in bulk fluids and adsorption systems, Chem. Eng. J. 334 (2018) 1410–1421.
[48] D.D. Do, D. Nicholson, H.D. Do, On the Henry constant and isosteric heat at zero loading in gas phase adsorption, J. Colloid Interface Sci. 324 (1–2) (2008) 15–24.
[49] P. Phadungbut, V.T. Nguyen, D.D. Do, D. Nicholson, C. Tangsathitkulchai, On the phase transition in a monolayer adsorbed on graphite at temperatures below the 2D-critical temperature, Mol. Simul. 41 (5–6) (2014) 446–454.
[50] G. Brown, W. Ziegler, Vapor pressure and heats of vaporization and sublimation of liquids and solids of interest in cryogenics below 1-atm pressure, Springer, In Adv. Cryog. Eng., 1980, pp. 662–670.
[51] M. Sutton, S.G.J. Mochrie, R.J. Birgeneau, Direct observation of layer-by-layer wetting of graphite by ethylene, Physical Review Letters 51 (5) (1983) 407–410.
[52] W.A. Steele, Monolayers of Linear Molecules Adsorbed on the Graphite Basal Plane: Structures and Intermolecular Interactions, Langmuir 12 (1) (1996) 145–153.
[53] S.E. Hoory, J.M. Prausnitz, Adsorption of hydrocarbons on graphitized carbon, Transactions of the Faraday Society 63 (1967) 455–460.
[54] C. Fan, D.D. Do, D. Nicholson, A new and effective Bin-Monte Carlo scheme to study vapour–liquid equilibria and vapour–solid equilibria, Fluid Phase Equilib. 325 (2012) 53–65.
[55] J. Smukala, R. Span, W. Wagner, , New Equation of State for Ethylene Covering the Fluid Region for Temperatures From the Melting Line to 29 (5) (2000) 1053–1121, 450 K at Pressures up to 300 MPa.
[56] E.W. Lemmon, M.O. McLinden, D.G. Friend, Thermophysical Properties of Fluid Systems in NIST Chemistry WebBook, NIST Standard Reference Database Number 69, Gaithersburg, MD, National Institute of Standards and Technology, 2018.



View publication stats